Science Advances
AAAS

advances.sciencemag.org/cgi/content/full/7/29/eabf5620/DC1

Supplementary Materials for

Circuit mechanisms for the chemical modulation of cortex-wide network interactions and behavioral variability

Thomas Pfeffer*, Adrian Ponce-Alvarez, Konstantinos Tsetsos, Thomas Meindertsma, Christoffer Julius Gahnström, Ruud Lucas van den Brink, Guido Nolte, Andreas Karl Engel, Gustavo Deco, Tobias Hinrich Donner*

*Corresponding author. Email: thms.pfffr@gmail.com (T.P.); t.donner@uke.de (T.H.D.)

Published 16 July 2021, *Sci. Adv.* **7**, eabf5620 (2021)
DOI: 10.1126/sciadv.abf5620

The PDF file includes:

Other Supplementary Material for this manuscript includes the following:

(available at advances.sciencemag.org/cgi/content/full/7/29/eabf5620/DC1)

Movie S1

Supplementary Materials

Materials and Methods

Dynamics of a single-node Wilson Cowan model

The mass dynamics of the local nodes were governed by the control parameters and $\boldsymbol{b_E}$ and $\boldsymbol{b_I}$, representing external drive (background input) to the excitatory and inhibitory populations, respectively. The parameters of the model were tuned such that the model is in a dynamical state close to a so-called supercritical Adronov-Hopf bifurcation. The 'Hopf-bifurcation' separates a regime in which the system relaxes to a stable fixed point, or *focus*, by drawing a spiral in the phase space (noise-driven, damped oscillations; Fig. 2C; Fig. S6A, middle and bottom), and a regime in which the network activity settles into a *limit-cycle*, a closed orbit in the phase space corresponding to a periodic solution (sustained oscillations; Fig. 2C and Fig. S6A, top). When the system settles into the focus, intrinsic noise induces stochastic oscillations and gives rise to a broad spectral density with a single peak. In contrast, in the limit-cycle, autonomous regular oscillations are observed, with a spectral density presenting a narrow peak (see Fig. S6E for an average across several nodes). The parameters $\boldsymbol{w}$ as well as $\boldsymbol{b_E}$ and $\boldsymbol{b_I}$ were loosely adjusted in order to produce dynamics in the vicinity of a supercritical Hopf bifurcation. In the context of the Hopf-bifurcation, the term 'supercritical' is not to be confused with the same term referring to self-organized criticality and power law scaling behavior (*80*).

Linear noise approximation for two-nodes Wilson Cowan model

We used a linear noise approximation to study the linear fluctuations around the system's fixed points, i.e., $E_i = E_i^* + \delta E_i$ and $I_i = I_i^* + \delta I_i$, where the fixed points are given by:

$$E_i^* = \sigma\big(w_{EE}E_i^* - w_{EI}I_i^* + cE_j^* + b_E + \Delta b\big), \qquad \text{(Eq. 27)}$$

$$I_i^* = \sigma(w_{IE}E_i^* - w_{II}I_i^* + b_I + \Delta b). \qquad \text{(Eq. 28)}$$

Dynamic equations for the linear fluctuations can be written as:

$$\frac{d}{dt}\delta\boldsymbol{r} = \boldsymbol{A}\delta\boldsymbol{r} + \boldsymbol{\eta}, \qquad \text{(Eq. 29)}$$

where $\delta\boldsymbol{r} = [\delta E_1, \delta I_1, \delta E_2, \delta I_2]$, $\boldsymbol{\eta}$ is the noise matrix, and $\boldsymbol{A}$ is the Jacobian matrix of the system evaluated at the fixed points, given by the 4-by-4 matrix:

$$A_{\alpha\beta} = \left[\frac{1}{\tau_\alpha}\frac{\partial F_\alpha}{\partial \beta}\right]_{(E_1^*, I_1^*, E_2^*, I_2^*)}, \qquad \text{(Eq. 30)}$$

where $\alpha, \beta \in \{E_1, I_1, E_2, I_2\}$. Noting that $\sigma'(u) = g\sigma(u)[1 - \sigma(u)]$ and that, by symmetry, $E_1^* = E_2^* = E^*$ and $I_1^* = I_2^* = I^*$, we get:

$$A = \begin{bmatrix} A_{EE} & A_{EI} & K & 0 \\ A_{IE} & A_{II} & 0 & 0 \\ K & 0 & A_{EE} & A_{EI} \\ 0 & 0 & A_{IE} & A_{II} \end{bmatrix}, \quad \text{(Eq. 31)}$$

where:

$$\tau_E A_{EE} = -1 + w_{EE} g E^* (1 - E^*), \quad \text{(Eq. 32)}$$
$$\tau_E A_{EI} = -w_{EI} g E^* (1 - E^*), \quad \text{(Eq. 33)}$$
$$\tau_E K = c g E^* (1 - E^*), \quad \text{(Eq. 34)}$$
$$\tau_I A_{IE} = w_{IE} g I^* (1 - I^*), \quad \text{(Eq. 35)}$$
$$\tau_I A_{II} = -1 - w_{II} g I^* (1 - I^*), \quad \text{(Eq. 36)}$$

The stationary covariances $\boldsymbol{C_v} = \langle \delta \boldsymbol{r} \delta \boldsymbol{r^T} \rangle$ between all populations can be obtained through the Jacobian matrix, by solving the following equation:

$$\boldsymbol{A C_v} + \boldsymbol{C_v A^T} + \boldsymbol{Q_n} = 0, \quad \text{(Eq. 37)}$$

where $\boldsymbol{Q_n} = \langle \boldsymbol{\eta \eta^T} \rangle$ is the covariance matrix of the noise (which is diagonal for uncorrelated white noise) and the superscript *T* denotes the transpose operator. Note that the Jacobian matrix depends on the system's fixed points, i.e., it depends on the state of the nonlinear system and, thus, on the external inputs (b_E, b_I). Hence, the correlations are also a function of the parameters (b_E, b_I). Equation 37 can be solved using the eigen-decomposition of the Jacobian matrix evaluated at the fixed points: $A = LDL^{-1}$, where *D* is a diagonal matrix containing the eigenvalues of *A*, denoted λ_i, and the columns of matrix *L* are the eigenvectors of *A*. Multiplying Eq. 37 by L^{-1} from the left and by $L^{-\dagger}$ from the right (the superscript dagger being the conjugate transpose) we get:

$$\boldsymbol{C_v} = \boldsymbol{L M L^{\dagger}}, \quad \text{(Eq. 38)}$$

where $\boldsymbol{M}$ is given by: $M_{ij} = -\tilde{Q}_{ij}/(\lambda_i + \lambda_j^*)$, and $\boldsymbol{\tilde{Q}} = \boldsymbol{L^{-1} M L^{-\dagger}}$.

Supplementary Discussion

Assumptions for large-scale (Wilson Cowan) modeling

Our large-scale modeling approach was based on two assumptions. In the following, we discuss the physiological evidence supporting these assumptions.

Assumption 1. Cortex operates in a regime of noise driven, not sustained, oscillations. We assumed that the cerebral cortex generally operates in a regime of noise-driven oscillations, rather than self-sustained oscillations (Fig. 2C; Fig. S6A). In the noise-driven (also referred to as fluctuation-driven) regime, stochastic fluctuations in activity drive damped oscillations in the local nodes. Superposition of such damped oscillations, triggered at random moments in time, give rise to the same ongoing variations in the amplitude or the power of band-limited activity that are commonly observed in electrophysiological data under steady-state conditions (*33*, *81*), including the current data set (*28*). The time-varying power envelopes were used to compute the inter-regional correlations in the MEG data (Fig. S2). Consequently, we eliminated all parameter

combinations that fell outside of this regime of noise-driven oscillations from further consideration (see Methods for identification of the parameters producing sustained oscillations to be excluded).

Assumption 2. TASK increased the drive of both, E- and I-populations. We assumed that the change from REST to TASK corresponded to a shift of the model's dynamical regime in an upward-rightward direction in the $(\boldsymbol{b_E}, \boldsymbol{b_I})$-plane (Fig. 2C, area defined by dashed outline). This means that background input to both excitatory and inhibitory neural populations is increased for all nodes of the model. This assumption rests on the straightforward notion that our elementary visual task increased the input to sensory and task-related cortical regions. There is substantial evidence for the idea that cortical circuits generally operate in a regime of rough balance between excitation and inhibition (*42*, *82*). Specifically, sensory input increases not only feedforward excitation (i.e., feedforward drive of pyramidal cells), but also feedforward inhibition (i.e., feedforward drive of interneurons) in sensory cortex (*40*, *41*), and it is assumed that this motif repeats across the cortical hierarchy (*42*) likely augmented through circuit motifs for feedback inhibition (*83*). Correspondingly, we assumed that the visual task increased the background input to excitatory and inhibitory populations in a (loosely) balanced fashion, with a slight dominance of feedforward inhibition in the case of the cortex-wide model (see Fig. 2D,E). Indeed, recent evidence from rodent physiology shows that visual stimulation leads to a more pronounced inhibitory response (*39*, *84*) compared to the excitatory response, consistent with sensory input leading to even stronger feedforward inhibition compared to feedforward excitation. Note that this was in line with *Assumption 1*: if the task-induced increase in excitation was much larger than the task-induced increase in inhibition, the dynamical regime of the network would change to oscillatory, inconsistent with physiological evidence.

Simulation and fitting of cortex-wide Wilson Cowan model

The dynamical regime was defined as noise- or fluctuation-driven if: (1) the maximum and minimum were identical at any point in time or (2) the difference between maximum and minimum decreased monotonously over time (indicative of a damped oscillation). If none of the two were true, the signal was defined as a sustained oscillation. Note that this approach does not allow to distinguish between the two regimes with full certainty as the time scale with which the amplitude of an oscillation decays back to the fixed point increases as one approaches the Hopf-bifurcation from the fluctuation-driven regime (see Fig. S6A, middle and bottom panels). Thus, the closer the dynamical regime is to the Hopf-bifurcation, the more simulation time is required to accurately distinguish a sustained oscillation from a damped oscillation.

Microcircuit modeling (spiking neurons)

Microcircuit model of local node. We simulated the leaky integrate-and-fire circuit across a range of parameters to identify a stable working point where the network exhibits dynamics reminiscent of the "asynchronous state" (*85*). We defined the asynchronous state as being characterized by a low spontaneous firing rate (1-5 Hz) and low mean pairwise spike correlations ($r < 0.1$; averaged across all pairs of excitatory units). In addition, we identified a working point in the "synchronized state", where the pairwise spike correlations where relatively high ($r > 0.3$), but spontaneous firing rates were comparable to the asynchronous state. This was achieved by changing AMPA-mediated recurrent excitation as well as the GABA-mediated feedback inhibition in a multiplicative manner: we started from the baseline parameters of (*44*), with some minor changes (see Methods), and multiplied $g_{E\rightarrow E,AMPA}$ (i.e., conductance of recurrent AMPA receptors) and $g_{I\rightarrow E,GABA}$ (i.e., conductance of GABAergic feedback inhibition) with 24 and 12 (respectively) linearly spaced values, ranging from 0.2 to 5 and 2.7 to 5. Fig. S9A shows firing rates (left) and mean pairwise spike correlations (right) for all parameter combinations. While for

the main part of the analysis, we focus on the asynchronous state (shown in Fig. 2F; mean firing rate FR = 4.14 Hz; mean pairwise spike correlations r = 0.05), we further wanted to test whether the observed effect of feedback inhibition on response gain holds true also for the synchronous state. To this end, we first identified a dynamical regime reminiscent of the synchronous state, with low firing rates (FR = 5.11 Hz) but relatively high pairwise spike correlations (r = 0.27). We find that, irrespective of state, a reduction in feedback inhibition leads to an increase in response gain (Fig. S9B).

Tuning of parameters of decision circuit model. This model was based on a circuit model of decision-making developed to explain neural dynamics and choice behavior in standard two-alternative forced choice tasks, entailing trials of a few seconds of duration (*44*). Without further adjustments to the parameters of the decision circuit, the network dynamics would rapidly enter one of the two possible attractor states, reflecting the preference for decision 1 or decision 2. Moreover, without sufficient levels of external drive or noise, the network would dwell in those states indefinitely, as the lateral inhibition would dominate over the external input or the magnitude of the noise. In order to introduce dynamics that exceed beyond short timescales (single trials), we increased the level of background noise as well as the strength of the external stimulus. This way, we identified a state where the model would switch continuously between two attractors. Once this point was identified, we only changed feedback inhibition in order to assess the influence of E/I ratio on perceptual transitions (Fig. 3C).

Note that other studies that employed neural circuit models similar to the one used here for the study of perceptual fluctuations during ambiguous stimulations (*86*) also included adaptation as an alternative mechanistic explanation for perceptual transitions. For the sake of simplicity, we did not consider this in the current circuit.

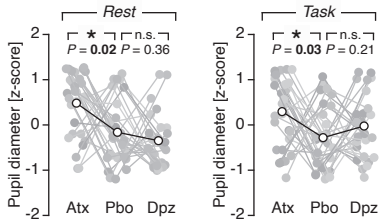

Fig. S1. Drug effect on baseline pupil diameter. Baseline pupil diameter after the administration of atomoxetine (Atx), placebo (Pbo) or donepezil (Dpz), separately for rest (left) and task (right). (*) indicates $P < 0.05$ (two-sided paired permutation test).

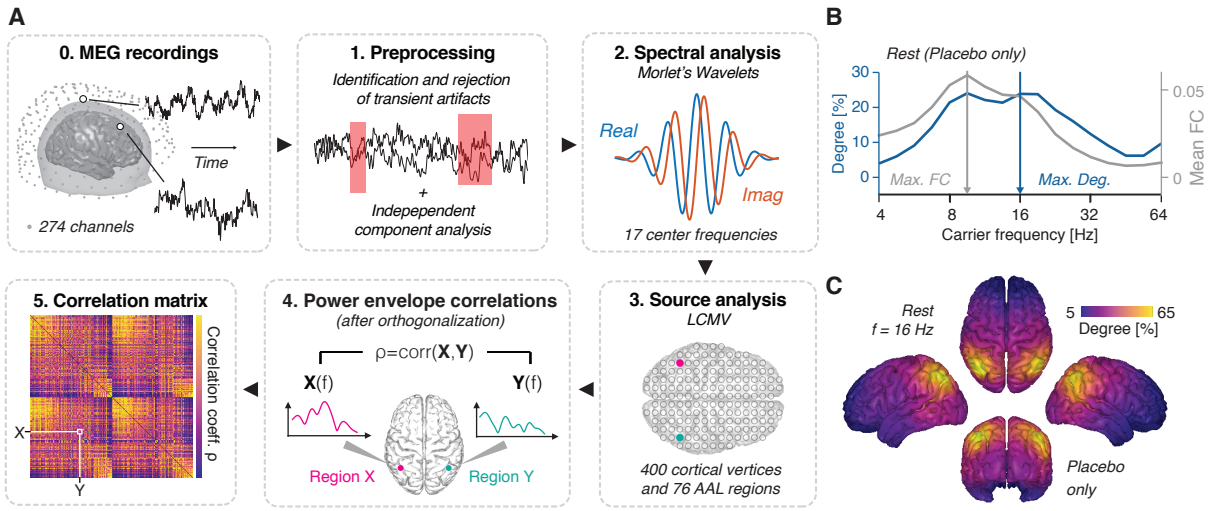

Fig. S2. Quantifying cortex-wide functional connectivity. (A) (0.) Whole-head magnetoencephalography (MEG) was recorded using 274 recording channels located in a helmet above the participants head**. (**1.) The sensor-level signal was cleaned from transient and sustained artifacts (e.g. muscle and heart beat artifacts, respectively). **(**2.) Spectral estimates were obtained from the cleaned sensor-level signal using complex wavelet convolution. **(**3.) From the spectral estimates and individual head models, source level power time series were obtained, **(**4.) from which orthogonalized power envelope correlations were computed. (5.) This resulted in functional connectivity (FC) matrices for each of the 17 carrier frequency bands of interest. **(B)** Global degree (see Methods) and mean FC as a function of frequency during the rest-placebo condition. **(C)** Spatial map of degree during the rest-placebo condition**.** Correlations peak in the 'alpha' (center frequency 9.51 Hz; B) and 'beta' frequency range (center frequency 16 Hz; B), with strongest 'connectedness' (degree) in left and right posterior parietal cortex. These results are consistent with previous reports using an analogous approach to resting-state MEG data.

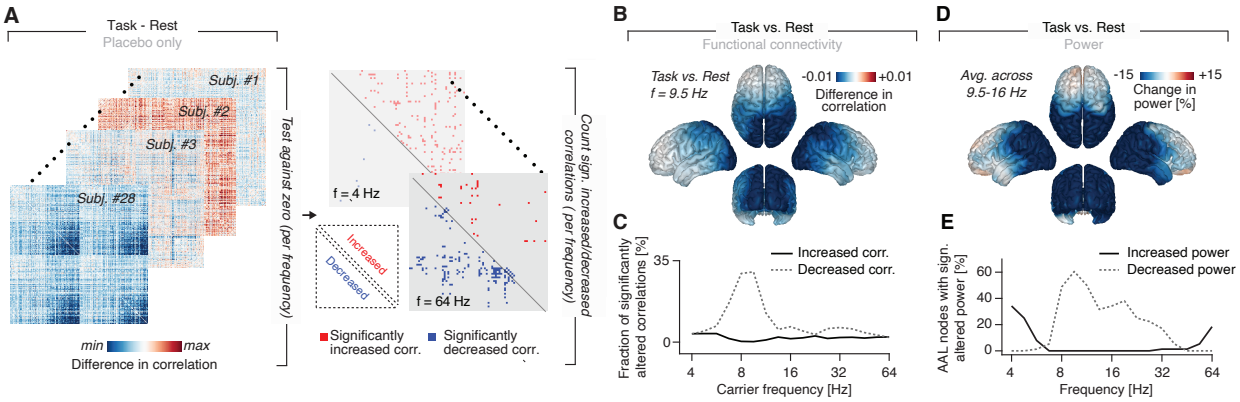

Fig. S3. Quantifying task effects on functional connectivity. (A) Illustration of the approach to quantify changes in the global activity correlation structure: First, the difference between two conditions (here: rest and task; placebo only) was tested by means of a two-sided paired t-test. Next, the number of statistically significantly ($P < 0.05$; uncorrected) increased (in red) and significantly decreased (in blue) connections was counted. **(B)** Spatial distribution of the difference in correlation between task and rest (placebo only) at a carrier frequency of 9.5 Hz. **(C)** The fraction of significantly ($P < 0.05$, two-sided paired t-test) altered correlations (negative and positive alterations) can be computed for each frequency band of interest, resulting in a spectrum of fraction of significantly altered correlations. **(D)** Spatial distribution of the difference in power between task and rest (placebo only), averaged across the frequency range from 9.5 to 16 Hz. **(E)** The fraction of nodes (in this case: AAL nodes; see Methods) with significantly altered power (negative and positive alterations; $P < 0.05$, two-sided paired t-test) can be computed for each frequency band of interest, resulting in a spectrum of fraction of nodes with significantly altered power.

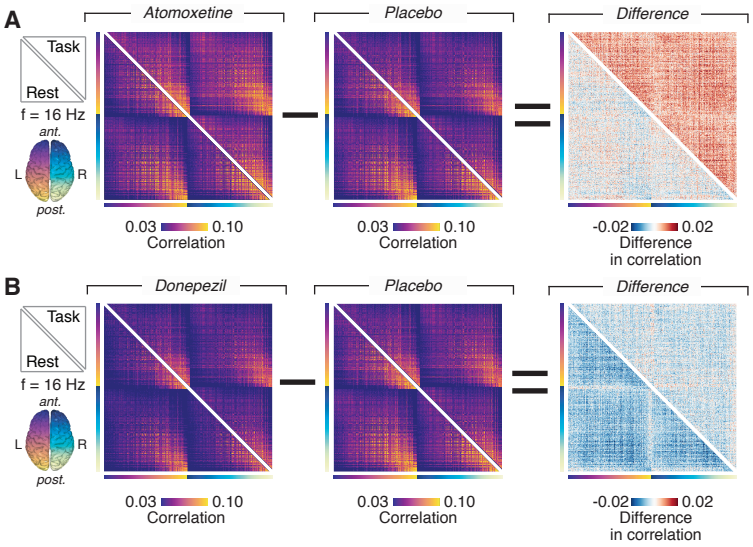

Fig. S4. Quantifying drug effects on functional connectivity. (A) Functional connectivity matrices (only lower or upper triangular parts; at a carrier frequency of 16 Hz) for atomoxetine, placebo and the difference between the two (lower triangular part: during rest; upper triangular part: during task) and **(B)** for donepezil, placebo and the difference between the two.

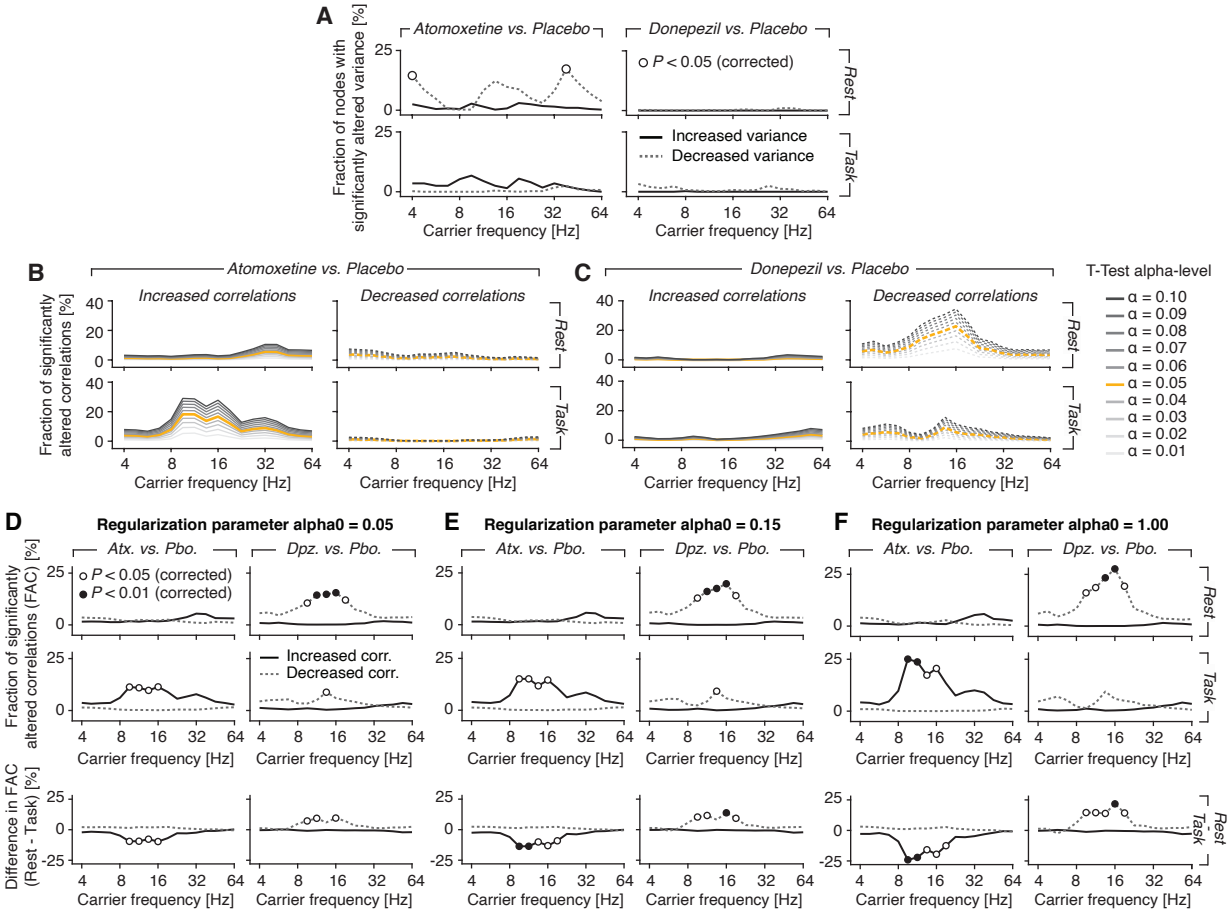

Fig. S5. The drug effects on functional connectivity are not driven by changes in variance and are not specific to certain analysis parameters. (A) Atomoxetine (left) induced a weak reduction in power envelope variance compared to placebo during rest (open circles indicate $P < 0.05$, two-sided paired single threshold permutation test). Atomoxetine produced a tendency towards the opposite effect during task (increase in local variance) during task, albeit not statistically significant. Donepezil (right) did not lead to any significant alterations in local power envelope variance. The pattern of local variance changes under atomoxetine (decrease during rest, increase during task) cannot explain the observed pattern of changes in correlations under atomoxetine (no effect during rest, increase during task). In particular, an increase in local variance during task would reduce, not increase, correlations, because the local variance enters in the denominator in the computation of the correlation coefficient. **(B-C)** The choice of the alpha-level for the initial paired t-test (Fig. 1E) does not affect the general qualitative pattern of the drug-induced changes in the fraction of significantly altered correlations. **(B)** Fraction of altered correlations as in Fig. 1E, but for various different alpha-values (for the initial t-test; see Methods), ranging from 0.01 to 0.10, for atomoxetine and **(C)** donepezil. **(D-F)** Fraction of significantly altered correlations (FAC; as in Fig. 1E) for different regularization parameters used for the source reconstruction procedure (see Methods; panel D: $\alpha = 0.05$; panel E: $\alpha = 0.15$; panel F: $\alpha = 1.00$). In the top row, the drug effects during rest are shown, in the middle row the effects during task (*Left:* Atomoxetine vs. placebo; *Right:* donepezil vs. placebo). The bottom row shows the effect of behavioral state (or context), i.e., the difference between the drug effect during Rest and the drug effect during Task. Significant differences are indicated by open circles ($P < 0.05$) and filled circles ($P < 0.01$; two-sided paired single-threshold permutation test).

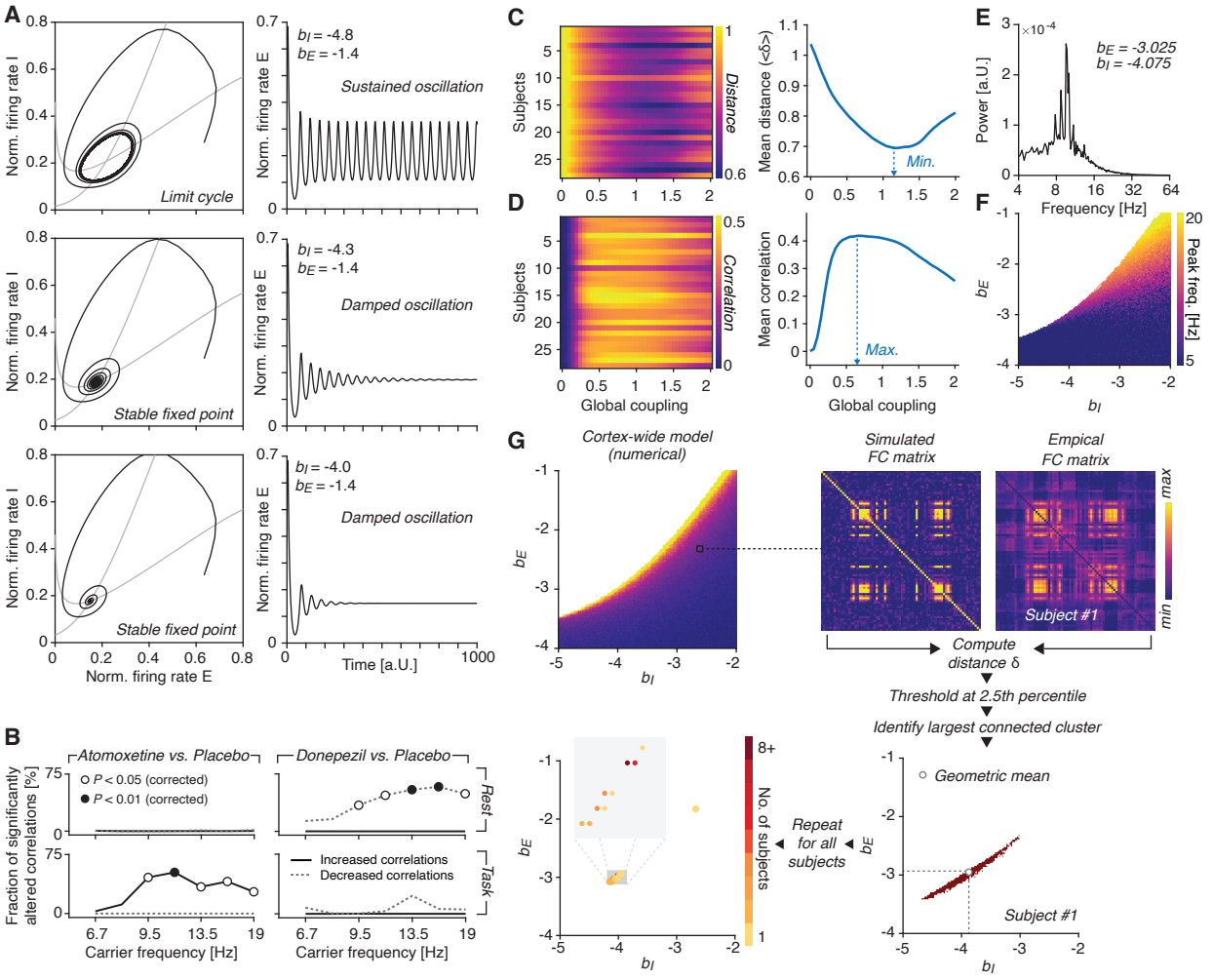

Fig. S6. Dynamics of the Wilson-Cowan models and fitting procedure of the cortex-wide model. (A) Dynamics of a single Wilson-Cowan node around the Hopf-bifurcation. *Top:* Dynamics in the oscillatory regime, exhibiting sustained oscillations. *Middle and bottom:* Dynamics in the noise-driven regime, exhibiting damped oscillations. **(B)** The drug effects on fraction of significantly altered correlations for 76 AAL nodes and selected carrier frequency bands (ranging from ~6.7 to ~19 Hz). **(C)** Estimation of the global coupling parameter. *Left:* across all participants and a number of background input parameters (to E and I), the similarity (here: distance; see Methods) between the simulated and the empirical functional connectivity matrices was computed. *Right:* Distance (averaged across participants) for various levels of global coupling. **(D)** Same as (C), but for Pearson correlation. **(E)** Averaged model power spectrum (averaged across all 76 nodes). **(F)** Peak frequency of the model for various levels of background inputs to E and I. **(G)** Illustration of the fitting procedure: for each combination of background inputs to E and I, as well as every participant, the distance between simulated and empirical FC (rest and placebo only) was computed. The resulting distance matrix was thresholded at the 2.5th percentile (all values larger were set to zero, all others to 1) and the largest connected cluster was identified. The geometric mean of this cluster was defined as the best-fitting value for a given participant. Repeating this procedure for all participants resulted in 28 fitted resting state parameters.

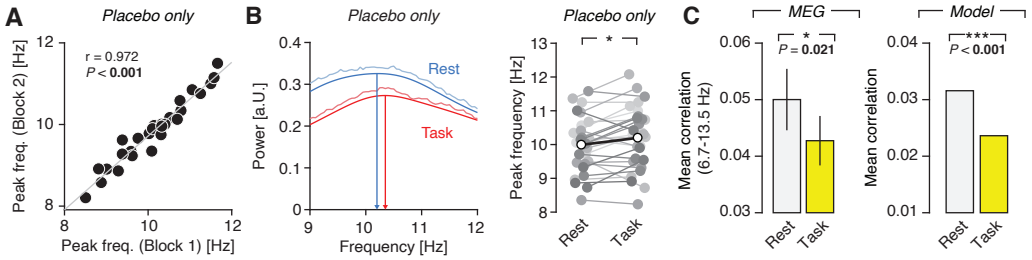

Fig. S7. Task alters alpha peak frequency and functional connectivity. **(A)** The estimated peak frequencies in the alpha-range (6-14 Hz) are highly consistent between the two recording blocks. **(B)** *Left:* The frequency peak in the averaged power spectrum fits (after subtracting the 1/f component) shifts towards slightly higher frequencies during task (red) compared to rest (blue). Darker colors: model fits; lighter colors: MEG data. *Right:* Task increases alpha peak frequency across subjects. **(C)** Mean correlation (averaged across all region pairs) is decreased during task compared to rest, both in the MEG (left; averaged across the alpha-/beta-range, 9.51 – 16 Hz, where the MEG exhibits peak correlations; see Fig. S2B) and the model (right). P-values: two-sided paired permutation test (100.000 permutations).

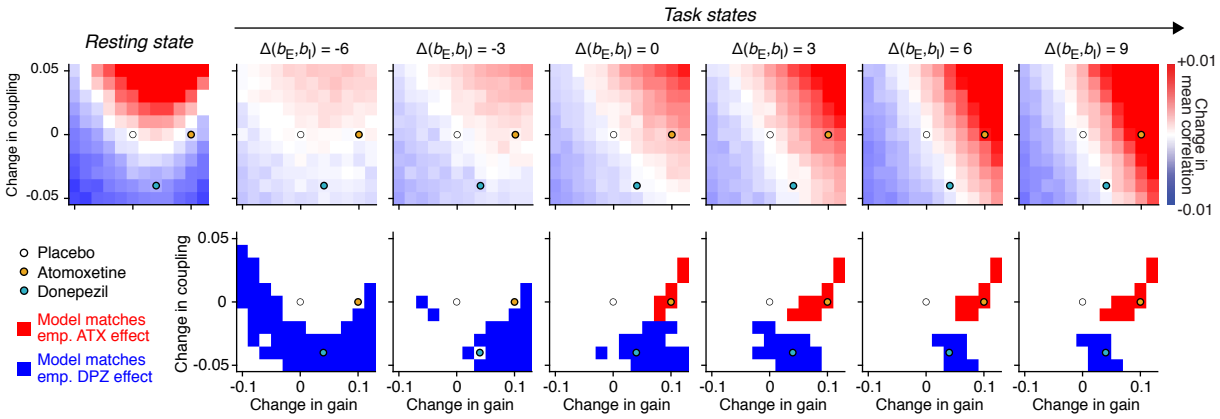

Fig. S8. Model consistency with empirical data across the parameter space. *Top row:* Difference in mean correlation (averaged across the upper triangular part of the 76x76 correlation matrix) across changes in gain and global coupling, for a number of task-related input strengths (plot in the center, where $\Delta(b_E, b_I) = 0$ corresponds to the input level shown in Fig. 2D,E, yellow circle). *Bottom row:* Corresponding binary masks highlighting the regions in the parameter space where the changes in mean correlation are qualitatively consistent with the empirical observations (Fig. 1E,F).

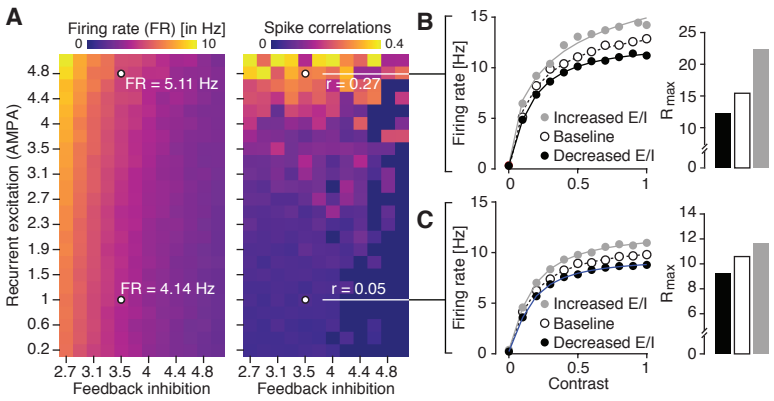

Fig. S9. Increased E/I ratio increases response gain in asynchronous and synchronous states. **(A)** The parameters of the leaky integrate-and-fire model were tuned such that the network dynamics are indicative of a synchronized state (depicted pairwise spike count correlations r = 0.27) and low baseline firing rate (depicted FR = 5.11 Hz) or an asynchronous regime (pairwise spike count correlations r = 0.05), with comparable baseline firing rate (FR = 4.14 Hz). **(B)** The effects of altered feedback inhibition on response gain in the synchronous regime **(C)** Same as (B), but for the asynchronous regime (identical to Fig. 2F, replotted here for better comparison).

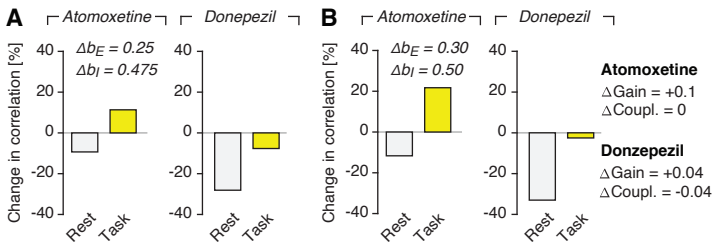

Fig. S10. Model with heterogeneous task-related inputs. Results from a model where only a subset of nodes (with significantly decreased power in the alpha-/beta range; see Methods) received task-related input. **(A)** Effects of changes in gain and global coupling (both equivalent to Fig. 2D,E) on the mean correlation, for task-related input strength equivalent to Fig. 2D,E. **(B)** Same as (A), but with slightly increased task-related inputs.

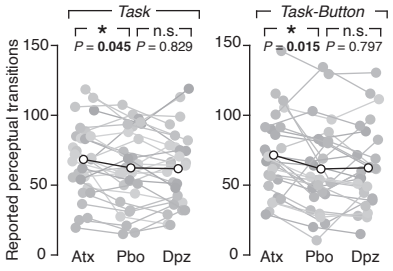

Fig. S11. Reported perceptual transitions during task and task-pressing. *Left*: Number of reported perceptual transitions after the administration of atomoxetine (Atx), placebo (Pbo) or donepezil (Dpz), separately for task (silent counting of perceptual transitions). *Right*: same for task-button (perceptual transitions reported through pressing a button; right) (*) indicates $P < 0.05$ (two-sided paired permutation test).

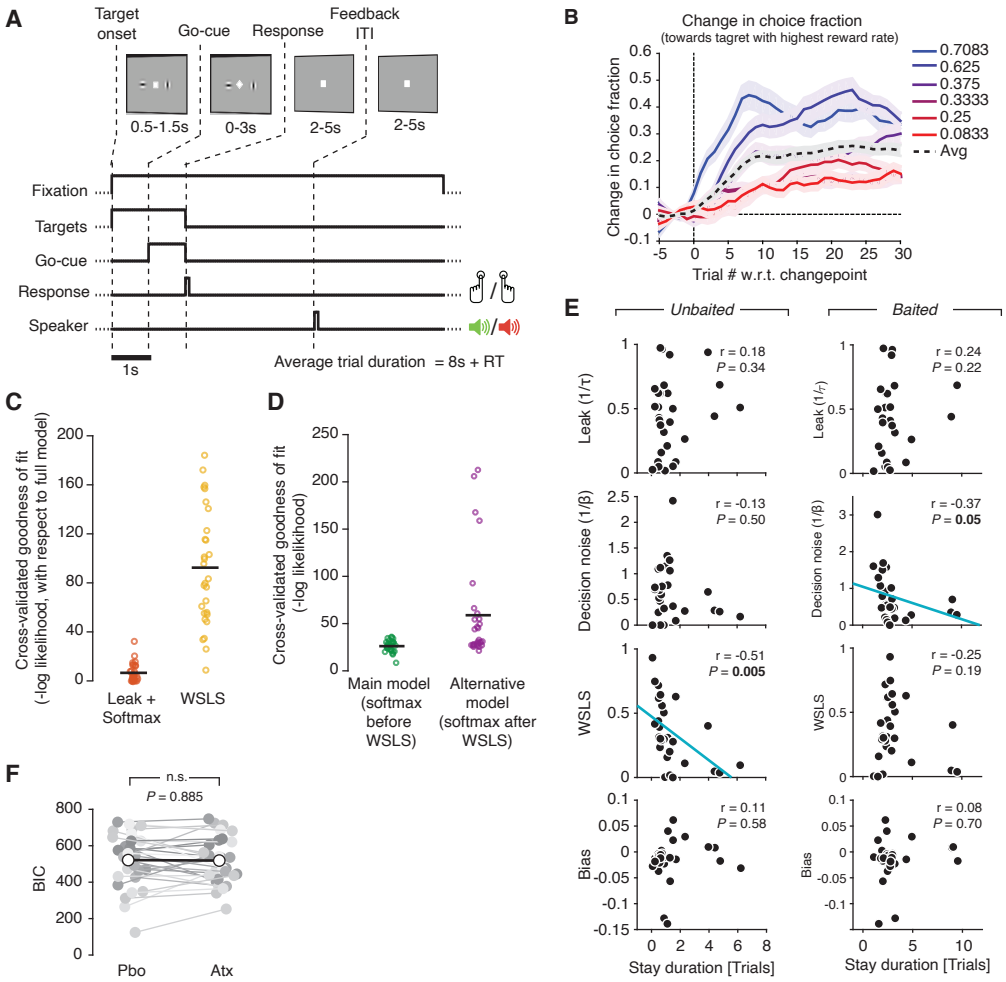

Fig. S12. Task design, behavior, and behavioral modeling for dynamic foraging task. (A) Behavioral task. Top: sequence of events during each trial. Two choice targets (vertical/horizontal Gabors, randomized location) are presented at trial onset. A go-cue (change of fixation marker) instructs subjects to indicate their choice, by pressing a button with left or right index finger. Binary auditory feedback (reward or no-reward) is delivered after variable delay. **(B)** Change-point triggered change in choice fraction. **(C)** Cross-validated comparison between behavioral model from main Fig. 4F with a model entailing only WSLS or only leaky reward integration combined with softmax transformation. The latter fits the data better, indicating that a reward integration mechanism is needed to account for the data. **(D)** Cross-validated comparison between behavioral model from main Fig. 4F and a model, in which softmax transformation of choice probability is applied after combination with WSLS heuristic. The model from Fig. 4F (softmax transformation before WSLS) fits the data better. **(E)** Correlations between individual's stay durations (where a "stay" is defined as the length of an uninterrupted sequence of choices to a stimulus with the same tilt, i.e., horizontal or vertical) and the estimated model parameters. **(F)** Comparison of the BIC values obtained from fitting the model to the placebo and the atomoxetine condition. P-value was obtained from a two-sided paired permutation test (100.000 permutations).

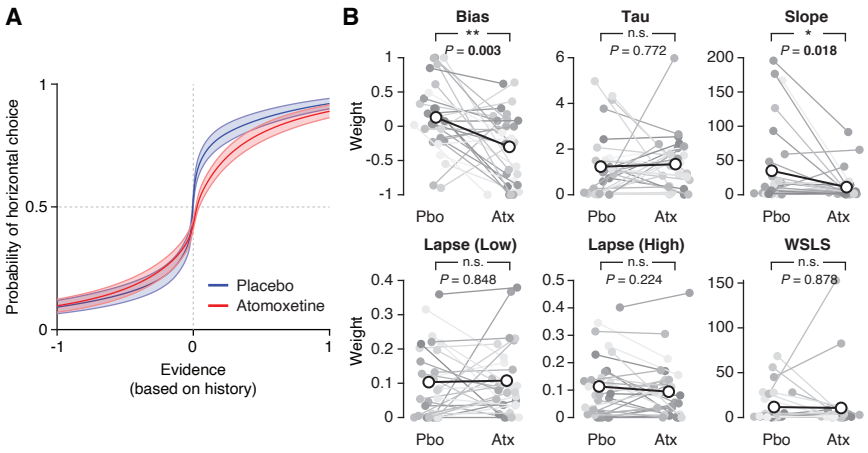

Fig. S13. Logistic regression analysis of choice behavior in foraging task. (A) Psychometric function for placebo (blue) and atomoxetine (red). **(B)** Comparison between regression model parameter estimates for atomoxetine vs. placebo. Timescale (tau) was obtained from an exponential fit to the outcome regressor weights as a function of previous trials (Methods). (*) $P < 0.05$; (**) $P < 0.01$; Two-sided paired permutation test (100.000 permutations).

Previous neurological or psychiatric diagnosis
Currently (or within 2 months prior to the start of the experiment) on medication that potentially alters brain activity
MRI or MEG incompatible implants
Pacemaker
Diagnosed cardiovascular disorder
Known hypersensitivity to atomoxetine or donepezil
Symptoms of significant mental or physical exhaustion
Other significant health-related issues
Regular smoker
Consumption of illegal substances
Consumption of 15 or more glasses of alcohol per week
Pregnancy

Table S1. Participant exclusion criteria

REGION INDEX	AAL REGION NAME	REGION INDEX	AAL REGION NAME
1	Precentral_L	**39**	Temporal_Inf_R
2	Frontal_Sup_L	**40**	Temporal_Pole_Mid_R
3	Frontal_Sup_Orb_L	**41**	Temporal_Mid_R
4	Frontal_Mid_L	**42**	Temporal_Pole_Sup_R
5	Frontal_Mid_Orb_L	**43**	Temporal_Sub_R
6	Frontal_Inf_Oper_L	**44**	Heschl_R
7	Frontal_Inf_Tri_L	**45**	Paracentral_Lobule_R
8	Frontal_Inf_Orb_L	**46**	Precuneus_R
9	Rolandic_Oper_L	**47**	Angular_R
10	Supp_Motor_Area_L	**48**	SupraMarginal_R
11	Frontal_Supp_Medial_L	**49**	Parietal_Inf_R
12	Frontal_Med_Orb_L	**50**	Parietal_Sup_R
13	Rectus_L	**51**	Postcentral_R
14	Cingulum_Ant_L	**52**	Fusiform_R
15	Cingulum_Mid_L	**53**	Occipital_Inf_R
16	Cingulum_Post_L	**54**	Occipital_Mid_R
17	Hippocampus_L	**55**	Occipital_Sup_R
18	ParaHippocampal L	**56**	Lingual_R
19	Calcarine_L	**57**	Cuneus_R
20	Cuneus_L	**58**	Calcarine_R
21	Lingual_L	**59**	ParaHippocampal_R
22	Occipital_Sup_L	**60**	Hippocampus_R
23	Occipital_Mid_L	**61**	Cingulum_Post_R
24	Occipital_Inf_L	**62**	Cingulum_Mid_R
25	Fusiform_L	**63**	Cingulum_Ant_R
26	Postcentral_L	**64**	Rectus_R
27	Parietal_Sup_L	**65**	Frontal_Med_Orb_R
28	Parietal_Inf_L	**66**	Frontal_Supp_Medial_R
29	SupraMarginal_L	**67**	Supp_Motor_Area__
30	Angular_L	**68**	Rolandic_Oper_R
31	Precuneus_L	**69**	Frontal_Inf_Orb_R
32	Paracentral_Lobule_L	**70**	Frontal_Inf_Tri_R
33	Heschl_L	**71**	Frontal_Inf_Oper_R
34	Temporal_Sub_L	**72**	Frontal_Mid_Orb_R
35	Temporal_Pole_Sup_L	**73**	Frontal_Mid_R
36	Temporal_Mid_L	**74**	Frontal_Sup_Orb_R
37	Temporal_Pole_Mid_L	**75**	Frontal_Sup_R
38	Temporal_Inf_L	**76**	Precentral_R

Table S2. List of cortical AAL regions included in the model-based analysis.

Movie S1. The 3D-Structure-from-Motion stimulus presented to the participants during the visual task (https://youtu.be/HzwC2CnVzT0)

REFERENCES AND NOTES

1. G. Aston-Jones, J. D. Cohen, An integrative theory of locus coeruleus-norepinephrine function: Adaptive gain and optimal performance. *Annu. Rev. Neurosci.* **28**, 403–450 (2005).

2. K. D. Harris, A. Thiele, Cortical state and attention. *Nat. Rev. Neurosci.* **12**, 509–523 (2011).

3. T. W. Robbins, A. F. T. Arnsten, The neuropsychopharmacology of fronto-executive function: Monoaminergic modulation. *Annu. Rev. Neurosci.* **32**, 267–287 (2009).

4. L. A. Schwarz, L. Luo, Organization of the locus coeruleus-norepinephrine system. *Curr. Biol.* **25**, R1051–R1056 (2015).

5. R. L. van den Brink, T. Pfeffer, T. H. Donner, Brainstem modulation of large-scale intrinsic cortical activity correlations. *Front. Hum. Neurosci.* **13**, 340 (2019).

6. R. L. van den Brink, T. Pfeffer, C. M. Warren, P. R. Murphy, K.-D. Tona, N. J. A. van der Wee, E. Giltay, M. S. van Noorden, S. A. R. B. Rombouts, T. H. Donner, S. Nieuwenhuis, Catecholaminergic neuromodulation shapes intrinsic MRI functional connectivity in the human brain. *J. Neurosci.* **36**, 7865–7876 (2016).

7. R. L. van den Brink, S. Nieuwenhuis, T. H. Donner, Amplification and suppression of distinct brainwide activity patterns by catecholamines. *J. Neurosci.* **38**, 7476–7491 (2018).

8. J. Turchi, C. Chang, F. Q. Ye, B. E. Russ, D. K. Yu, C. R. Cortes, I. E. Monosov, J. H. Duyn, D. A. Leopold, The basal forebrain regulates global resting-state fMRI fluctuations. *Neuron* **97**, 940–952.e4 (2018).

9. J. T. Coull, C. Büchel, K. J. Friston, C. D. Frith, Noradrenergically mediated plasticity in a human attentional neuronal network. *NeuroImage* **10**, 705–715 (1999).

10. A. J. Yu, P. Dayan, Uncertainty, neuromodulation, and attention. *Neuron* **46**, 681–692 (2005).

11. P. R. Montague, S. E. Hyman, J. D. Cohen, Computational roles for dopamine in behavioural control. *Nature* **431**, 760–767 (2004).

12. D. Servan-Schreiber, H. Printz, J. D. Cohen, A network model of catecholamine effects: Gain, signal-to-noise ratio, and behavior. *Science* **249**, 892–895 (1990).

13. E. Eldar, J. D. Cohen, Y. Niv, The effects of neural gain on attention and learning. *Nat. Neurosci.* **16**, 1146–1153 (2013).

14. A. A. Disney, C. Aoki, M. J. Hawken, Gain modulation by nicotine in macaque V1. *Neuron* **56**, 701–713 (2007).

15. J. L. Herrero, M. J. Roberts, L. S. Delicato, M. A. Gieselmann, P. Dayan, A. Thiele, Acetylcholine contributes through muscarinic receptors to attentional modulation in V1. *Nature* **454**, 1110–1114 (2008).

16. L. M. Hurley, D. M. Devilbiss, B. D. Waterhouse, A matter of focus: Monoaminergic modulation of stimulus coding in mammalian sensory networks. *Curr. Opin. Neurobiol.* **14**, 488–495 (2004).

17. P.-O. Polack, J. Friedman, P. Golshani, Cellular mechanisms of brain state-dependent gain modulation in visual cortex. *Nat. Neurosci.* **16**, 1331–1339 (2013).

18. M. A. Silver, A. Shenhav, M. D'Esposito, Cholinergic enhancement reduces spatial spread of visual responses in human early visual cortex. *Neuron* **60**, 904–914 (2008).

19. M. J. Roberts, W. Zinke, K. Guo, R. Robertson, J. S. McDonald, A. Thiele, Acetylcholine dynamically controls spatial integration in marmoset primary visual cortex. *J. Neurophysiol.* **93**, 2062–2072 (2005).

20. C. Y. Hsieh, S. J. Cruikshank, R. Metherate, Differential modulation of auditory thalamocortical and intracortical synaptic transmission by cholinergic agonist. *Brain Res.* **880**, 51–64 (2000).

21. G. Deco, A. Ponce-Alvarez, P. Hagmann, G. L. Romani, D. Mantini, M. Corbetta, How local excitation-inhibition ratio impacts the whole brain dynamics. *J. Neurosci.* **34**, 7886–7898 (2014).

22. J. M. Shine, R. L. van den Brink, D. Hernaus, S. Nieuwenhuis, R. A. Poldrack, Catecholaminergic manipulation alters dynamic network topology across cognitive states. *Netw. Neurosci.* **2**, 381–396 (2018).

23. K. A. Ferguson, J. A. Cardin, Mechanisms underlying gain modulation in the cortex. *Nat. Rev. Neurosci.* **21**, 80–92 (2020).

24. R. C. Froemke, Plasticity of cortical excitatory-inhibitory balance. *Annu. Rev. Neurosci.* **38**, 195–219 (2015).

25. B. K. Murphy, K. D. Miller, Multiplicative gain changes are induced by excitation or inhibition alone. *J. Neurosci.* **23**, 10040–10051 (2003).

26. A. R. O. Martins, R. C. Froemke, Coordinated forms of noradrenergic plasticity in the locus coeruleus and primary auditory cortex. *Nat. Neurosci.* **18**, 1483–1492 (2015).

27. R. C. Froemke, M. M. Merzenich, C. E. Schreiner, A synaptic memory trace for cortical receptive field plasticity. *Nature* **450**, 425–429 (2007).

28. T. Pfeffer, A.-E. Avramiea, G. Nolte, A. K. Engel, K. Linkenkaer-Hansen, T. H. Donner, Catecholamines alter the intrinsic variability of cortical population activity and perception. *PLoS Biol.* **16**, e2003453 (2018).

29. F. P. Bymaster, J. S. Katner, D. L. Nelson, S. K. Hemrick-Luecke, P. G. Threlkeld, J. H. Heiligenstein, S. M. Morin, D. R. Gehlert, K. W. Perry, Atomoxetine increases extracellular levels of norepinephrine and dopamine in prefrontal cortex of rat: A potential mechanism for efficacy in attention deficit/hyperactivity disorder. *Neuropsychopharmacology* **27**, 699–711 (2002).

30. J. Reimer, M. J. McGinley, Y. Liu, C. Rodenkirch, Q. Wang, D. A. McCormick, A. S. Tolias, Pupil fluctuations track rapid changes in adrenergic and cholinergic activity in cortex. *Nat. Commun.* **7**, 13289 (2016).

31. S. Joshi, Y. Li, R. M. Kalwani, J. I. Gold, Relationships between pupil diameter and neuronal activity in the locus coeruleus, colliculi, and cingulate cortex. *Neuron* **89**, 221–234 (2016).

32. J. W. de Gee, O. Colizoli, N. A. Kloosterman, T. Knapen, S. Nieuwenhuis, T. H. Donner, Dynamic modulation of decision biases by brainstem arousal systems. *eLife* **6**, e23232 (2017).

33. J. F. Hipp, D. J. Hawellek, M. Corbetta, M. Siegel, A. K. Engel, Large-scale cortical correlation structure of spontaneous oscillatory activity. *Nat. Neurosci.* **15**, 884–890 (2012).

34. D. Leopold, N. Logothetis, Multistable phenomena: Changing views in perception. **3**, 254–264 (1999).

35. J. Cohen, *Statistical Power Analysis for the Behavioral Sciences* (Routledge, ed. 2, 1988).

36. H. R. Wilson, J. D. Cowan, Excitatory and inhibitory interactions in localized populations of model neurons. *Biophys. J.* **12**, 1–24 (1972).

37. X.-J. J. Wang, Neurophysiological and computational principles of cortical rhythms in cognition. **90**, 1195–1268 (2010).

38. G. Spyropoulos, J. R. Dowdall, M. L. Schölvinck, C. A. Bosman, B. Lima, A. Peter, I. Onorato, J. Klon-Lipok, R. Roese, S. Neuenschwander, W. Singer, M. Vinck, P. Fries, Spontaneous variability in gamma dynamics described by a linear harmonic oscillator driven by noise. *bioRxiv*, 793729 (2020).

39. B. Haider, M. Häusser, M. Carandini, Inhibition dominates sensory responses in the awake cortex. *Nature* **493**, 97–100 (2013).

40. J. S. McCasland, L. S. Hibbard, GABAergic neurons in barrel cortex show strong, whisker-dependent metabolic activation during normal behavior. *J. Neurosci.* **17**, 5509–5527 (1997).

41. H. A. Swadlow, Thalamocortical control of feed-forward inhibition in awake somatosensory “barrel” cortex. *Philos. Trans. R. Soc. Lond. Ser. B Biol. Sci.* **357**, 1717–1727 (2002).

42. M. N. Shadlen, W. T. Newsome, The variable discharge of cortical neurons: Implications for connectivity, computation, and information coding. *J. Neurosci.* **18**, 3870–3896 (1998).

43. A. Renart, C. K. Machens, Variability in neural activity and behavior. *Curr. Opin. Neurobiol.* **25**, 211–220 (2014).

44. X.-J. Wang, Probabilistic decision making by slow reverberation in cortical circuits. *Neuron* **36**, 955–968 (2002).

45. N. H. Lam, T. Borduqui, J. Hallak, A. C. Roque, A. Anticevic, J. H. Krystal, X.-J. Wang, J. D. Murray, Effects of altered excitation-inhibition balance on decision making in a cortical circuit model. *bioRxiv*, 100347 (2017).

46. J. D. Cohen, S. M. McClure, A. J. Yu, Should I stay or should I go? How the human brain manages the trade-off between exploitation and exploration. *Philos. Trans. R. Soc. B* **362**, 933–942 (2007).

47. M. J. Frank, B. B. Doll, J. Oas-Terpstra, F. Moreno, Prefrontal and striatal dopaminergic genes predict individual differences in exploration and exploitation. *Nat. Neurosci.* **12**, 1062–1068 (2009).

48. R. Cools, Chemistry of the adaptive mind: Lessons from dopamine. *Neuron* **104**, 113–131 (2019).

49. L. P. Sugrue, G. S. Corrado, W. T. Newsome, Matching behavior and the representation of value in the parietal cortex. *Science* **304**, 1782–1787 (2004).

50. G. S. Corrado, L. P. Sugrue, H. S. Seung, W. T. Newsome, Linear-Nonlinear-Poisson models of primate choice dynamics. *J. Exp. Anal. Behav.* **84**, 581–617 (2005).

51. M. Usher, J. D. Cohen, D. Servan-Schreiber, J. Rajkowski, G. Aston-Jones, The role of locus coeruleus in the regulation of cognitive performance. *Science* **283**, 549–554 (1999).

52. G. Aston-Jones, J. Rajkowski, J. Cohen, Role of locus coeruleus in attention and behavioral flexibility. **46**, 1309–1320 (1999).

53. G. A. Kane, E. M. Vazey, R. C. Wilson, A. Shenhav, N. D. Daw, G. Aston-Jones, J. D. Cohen, Increased locus coeruleus tonic activity causes disengagement from a patch-foraging task. *Cogn. Affect. Behav. Neurosci.* **17**, 1073–1083 (2017).

54. D. G. R. Tervo, M. Proskurin, M. Manakov, M. Kabra, A. Vollmer, K. Branson, A. Y. Karpova, Behavioral variability through stochastic choice and its gating by anterior cingulate cortex. *Cell* **159**, 21–32 (2014).

55. C. M. Warren, R. C. Wilson, N. J. van der Wee, E. J. Giltay, M. S. van Noorden, J. D. Cohen, S. Nieuwenhuis, The effect of atomoxetine on random and directed exploration in humans. *PLOS ONE* **12**, e0176034 (2017).

56. C. Eisenegger, M. Naef, A. Linssen, L. Clark, P. K. Gandamaneni, U. Müller, T. W. Robbins, Role of dopamine D2 receptors in human reinforcement learning. *Neuropsychopharmacology* **39**, 2366–2375 (2014).

57. C. Findling, V. Skvortsova, R. Dromnelle, S. Palminteri, V. Wyart, Computational noise in reward-guided learning drives behavioral variability in volatile environments. *Nat. Neurosci.* **22**, 2066–2077 (2019).

58. J. J. Letzkus, S. B. E. Wolff, E. M. M. Meyer, P. Tovote, J. Courtin, C. Herry, A. Lüthi, A disinhibitory microcircuit for associative fear learning in the auditory cortex. *Nature* **480**, 331–335 (2011).

59. A. F. T. Arnsten, C. D. Paspalas, N. J. Gamo, Y. Yang, M. Wang, Dynamic network connectivity: A new form of neuroplasticity. *Trends Cogn. Sci.* **14**, 365–375 (2010).

60. M. D. Fox, M. Greicius, Clinical applications of resting state functional connectivity. *Front. Syst. Neurosci.* **4**, 19 (2010).

61. P. J. Tiseo, S. L. Rogers, L. T. Friedhoff, Pharmacokinetic and pharmacodynamic profile of donepezil HCl following evening administration: Evening administration of donepezil HCl. *Br. J. Clin. Pharmacol.* **46**, 13–18 (1998).

62. J.-M. Sauer, B. J. Ring, J. W. Witcher, Clinical pharmacokinetics of atomoxetine. *Clin. Pharmacokinet.* **44**, 571–590 (2005).

63. H. Wallach, D. N. O'connell, The kinetic depth effect. *J. Exp. Psychol.* **45**, 205–217 (1953).

64. D. H. Brainard, The psychophysics toolbox. *Spat. Vis.* **10**, 433–436 (1997).

65. T. Knapen, J. W. de Gee, J. Brascamp, S. Nuiten, S. Hoppenbrouwers, J. Theeuwes, Cognitive and ocular factors jointly determine pupil responses under equiluminance. *PLOS ONE* **11**, e0155574 (2016).

66. R. Oostenveld, P. Fries, E. Maris, J.-M. Schoffelen, FieldTrip: Open source software for advanced analysis of MEG, EEG, and invasive electrophysiological data. *Comput. Intell. Neurosci.* **2011**, 156869 (2011).

67. A. Hyvarinen, Fast and robust fixed-point algorithms for independent component analysis. *IEEE Trans. Neural Netw.* **10**, 626–634 (1999).

68. D. J. Hawellek, I. M. Schepers, B. Roeder, A. K. Engel, M. Siegel, J. F. Hipp, Altered intrinsic neuronal interactions in the visual cortex of the blind. *J. Neurosci.* **33**, 17072–17080 (2013).

69. B. D. Van Veen, W. van Drongelen, M. Yuchtman, A. Suzuki, Localization of brain electrical activity via linearly constrained minimum variance spatial filtering. *IEEE Trans. Biomed. Eng.* **44**, 867–880 (1997).

70. N. Tzourio-Mazoyer, B. Landeau, D. Papathanassiou, F. Crivello, O. Etard, N. Delcroix, B. Mazoyer, M. Joliot, Automated anatomical labeling of activations in SPM using a macroscopic anatomical parcellation of the MNI MRI single-subject brain. *NeuroImage* **15**, 273–289 (2002).

71. M. Rubinov, O. Sporns, Complex network measures of brain connectivity: Uses and interpretations. *NeuroImage* **52**, 1059–1069 (2010).

72. T. E. Nichols, A. P. Holmes, Nonparametric permutation tests for functional neuroimaging: A primer with examples. *Hum. Brain Mapp.* **15**, 1–25 (2002).

73. T. Donoghue, M. Haller, E. J. Peterson, P. Varma, P. Sebastian, R. Gao, T. Noto, A. H. Lara, J. D. Wallis, R. T. Knight, A. Shestyuk, B. Voytek, Parameterizing neural power spectra into periodic and aperiodic components. *Nat. Neurosci.* **23**, 1655–1665 (2020).

74. G. Deco, V. Jirsa, A. R. McIntosh, O. Sporns, R. Kotter, Key role of coupling, delay, and noise in resting brain fluctuations. *Proc. Natl. Acad. Sci. U.S.A.* **106**, 10302–10307 (2009).

75. G. Deco, J. Cruzat, J. Cabral, G. M. Knudsen, R. L. Carhart-Harris, P. C. Whybrow, N. K. Logothetis, M. L. Kringelbach, Whole-brain multimodal neuroimaging model using serotonin receptor maps explains non-linear functional effects of LSD. *Curr. Biol.* **28**, 3065–3074.e6 (2018).

76. M. Demirtaş, J. B. Burt, M. Helmer, J. L. Ji, B. D. Adkinson, M. F. Glasser, D. C. Van Essen, S. N. Sotiropoulos, A. Anticevic, J. D. Murray, Hierarchical heterogeneity across human cortex shapes large-scale neural dynamics. *Neuron* **101**, 1181–1194.e13 (2019).

77. D. F. M. Goodman, The Brian simulator. *Front. Neurosci.* **3**, 192–197 (2009).

78. K. Wimmer, A. Compte, A. Roxin, D. Peixoto, A. Renart, J. de la Rocha, Sensory integration dynamics in a hierarchical network explains choice probabilities in cortical area MT. *Nat. Commun.* **6**, 6177 (2015).

79. J. M. Beggs, D. Plenz, Neuronal avalanches in neocortical circuits. *J. Neurosci.* **23**, 11167–11177 (2003).

80. D. A. Leopold, Y. Murayama, N. K. Logothetis, Very slow activity fluctuations in monkey visual cortex: Implications for functional brain imaging. *Cereb. Cortex* **13**, 422–433 (2003).

81. C. van Vreeswijk, H. Sompolinsky, Chaos in neuronal networks with balanced excitatory and inhibitory activity. *Science* **274**, 1724–1726 (1996).

82. T. Womelsdorf, T. A. Valiante, N. T. Sahin, K. J. Miller, P. Tiesinga, Dynamic circuit motifs underlying rhythmic gain control, gating and integration. *Nat. Neurosci.* **17**, 1031–1039 (2014).

83. H. Adesnik, Synaptic mechanisms of feature coding in the visual cortex of awake mice. *Neuron* **95**, 1147–1159.e4 (2017).

84. A. Renart, J. Rocha, P. Bartho, L. Hollender, N. Parga, A. Reyes, K. D. Harris, The asynchronous state in cortical circuits. **327**, 587–590 (2010).

85. R. Moreno-Bote, J. Rinzel, N. Rubin, Noise-induced alternations in an attractor network model of perceptual bistability. *J. Neurophysiol.* **98**, 1125–1139 (2007).